ELSEVIER

Comput. Methods Appl. Mech. Engrg. 160 (1998) 71–88

Computer methods in applied mechanics and engineering

Three-dimensional simulations of Marangoni–Benard convection in small containers by the least-squares finite element method

Sheng-Tao Yu[a,*], Bo-Nan Jiang[b,1], Jie Wu[b,2], J.C. Duh[c,3]

[a]*Wayne State University, Detroit, MI 48202, USA*

[b]*ICOMP, OAI, NASA Lewis Research Center, Cleveland, OH 44135, USA*

[c]*NASA Lewis Research Center, Cleveland, OH 44135, USA*

Received 27 February 1998; accepted 18 August 1997

Abstract

This paper reports a numerical study of the Marangoni–Benard (MB) convection in a planar fluid layer. The least-squares finite element method (LSFEM) is employed to solve the three-dimensional Stokes equations and the energy equation. First, the governing equations are reduced to be first-order by introducing variables such as vorticity and heat fluxes. The resultant first-order system is then cast into a div–curl–grad formulation, and its ellipticity and boundary conditions are illustrated. This numerical approach provides an equal-order discretization for velocity, pressure, vorticity, temperature and heat conduction fluxes. Numerical results reported include the critical Marangoni numbers (M_{ac}) for the onset of the convection in containers with various aspect ratios, and the planforms of supercritical MB flows. The numerical solutions compared favorably with the experimental results reported by Koschmieder and Prahl.

1. Introduction

When a temperature gradient is applied orthogonally to a thin planar liquid layer with a free interface, cellular convection occurs from an originally quiescent state. The onset of the convection is due to the combined effects of the thermal stratification instability and the thermo-capillary effect. In particular, the temperature dependence of the surface tension on the free surface can destabilize the motionless fluid state to form regular convective cells. Usually, the diameters of these cells are in the same order of magnitude as compared to the depth of the fluid. This transport phenomenon is referred to as the Marangoni–Benard instability due to the first report of the flow phenomenon by Benard. The name also distinguishes it from the Rayleigh–Bernard instability which could occur without the free surface and is induced by buoyancy. In the past, extensive experimental studies of the MB convection using silicon oil as the working fluid have been conducted by Koschmieder and his coworkers [1–4]. Comprehensive reviews of the MB phenomena can be found in [5–7].

The theoretical studies of the MB convection have been focused on the stability analyses. The linear stability theory was first established by Pearson [8] and later on extended by Nield [9]. Since that time, other type analytical studies flourished, e.g. the energy stability theory [10] and the bifurcation theory [11,12]. While these studies have greatly enhanced our understanding of the flow physics, direct simulations of the flow phenomena remain attractive for further investigation. Full flow equations can be numerically solved without assumptions

* Corresponding author. Associate Professor (Research).

[1] Senior Research Associate.

[2] Senior Research Associate.

[3] Aerospace Scientist.

0045-7825/98/$19.00
PII: S0045-7825(97)00284-3

and simplifications usually employed in the stability analyses. The complications caused by the buoyancy for ground-based experiments can also be avoided. More than ever, the direct simulation is an indispensable tool for studying the regime of the supercritical MB flows where few studies have been conducted.

Duh [13] reported a two-dimensional numerical study of the MB flows. A method of stream function-vorticity was employed to simulate the MB rolls constrained by the bottom and two vertical peripheral walls. Numerical results of M_{ac} for the onset of convection as a function of the aspect ratio of the container (A_r) were reported. Here, A_r is defined as the ratio of the width of the container to the depth. Particularly, he found significant increase of M_{ax} when A_r is reduced to be less than two. Winters et al. [14] used a finite element method to solve the two-dimensional flow equations and they interpreted the numerical results by using the bifurcation theory. Similar to Duh's work, they also predicted the increase of M_{ac} for lower A_r.

Bestehorn [15] conducted the first three-dimensional calculation of the MB convection by a special method. He decomposed the divergence free velocity into a toroidal and a poloidal part. For fluids with large Prandtl numbers, the toroidal part of the velocity is null. As a result, the calculations were greatly simplified. By using this spectral treatment, Bestehorn showed the connection between the amplitude equations and the two-dimensional Ginzburg–Landau equation. He presented numerical results of the MB planforms in large containers without considering the wall effects.

By solving the primitive variables directly, Thess and Orszak [16,17] reported direct simulations of three-dimensional MB flows. Their numerical approach took advantage of the flow physics inherent in an infinite and periodic MB layer, i.e. the flow motion is solely determined by the temperature distribution on the free surface. Therefore, the calculation procedure was simplified and an efficient pseudo-spectral method was developed. The MB flows in both weakly and strongly supercritical regimes were reported. However, similar to Bestehorn's work, because of the assumption of the infinity and periodicity of the simulated MB cells, no wall effects were considered in Thess and Orszak's work.

In most practical systems, the working fluid is bounded by vertical walls, and the wall effects cannot be overlooked. For small containers, this situation is more pronounced. Rosenblat et al. [18,19] reported the first analytical study of the onset and the planforms of MB convection in small containers. Both linear and nonlinear stability analyses were conducted. A slippery lateral wall condition was employed to avoid the difficulty of the no-slip condition. By using a similar analytical method, Chen et al. [20] revisited this problem using the no-slip condition on the lateral walls. Both studies show a sharp increase of M_{ac} as A_r decreases below 2 and no significant increase of M_{ac} for $A_r \geqslant 2$. Similar conclusions have been reached by Duh using two-dimensional direct simulations. Recently, Koschmieder and Prahl [3] reported an experimental study of the onset and planforms of the MB convection in small circular and square containers. This study provided the physical evidence to confirm the strong increase of the M_{ac} as the A_r decreases to a small number. More than ever, they reported the post-onset Marangoni cells of unusual shapes not seen before when using large containers.

The objective of the present paper is to develop a new numerical approach to directly simulate the full three-dimensional MB convection. In particular, we like to include the peripheral wall effect. We concentrate our attention to the MB rolls in small square containers, and we want to recapture the unusual planforms observed by Koschmieder and Prahl [3]. Since the wall effect must be reckoned, the algorithms used by Bestehorn [15] and Thess et al. [16,17] cannot be employed. In the present paper, we used the least-squares finite element method (LSFEM) to solve the equations governing the flow physics of the MB convection.

The employed LSFEM is an extension of the work developed by Jiang and coworkers [21,22]. In [21], div–curl–grad formulations and their ellipticity for incompressible Navier–Stokes equations were derived. In [22], Jiang et al. showed that the LSFEM is optimal for the elliptic problems in the sense that the global error is of the same order of accuracy as compared to the approximation errors. Later on, the LSFEM has been extended by Yu et al. [23–25] to solve the compressible viscous flows at low Mach numbers and chemically reactive flows. In this work, we shall further extend the technique to calculate the MB convection.

The rest of the paper is organized as follows. In Section 2, we present the detailed derivation of the first-order formulation for the MB flows, including the non-dimensionalization, the div–curl–grad formulation, the ellipticity, and the boundary conditions. In Section 3, the LSFEM and the Jacobi conjugate gradient (JCG) method for solving the first-order equation set are elaborated. In Section 4, we report the numerical results of the MB flows inside small square containers. The calculation is set up according to the experiments conducted by Koschmieder and Prahl [3]. We then offer some concluding remarks.

2. Theoretical modeling

2.1. Governing equations and boundary conditions

In the present study, we like to recapture the MB planforms in square containers reported by Koschmieder and Prahl [3]. In Table 1, the properties of the silicon oil used in their experiments are listed.

According to these data, the Prandtl number of the silicon oil $P_r = \nu/\kappa$ is about 1000, and the capillary number $C = \rho\kappa\nu/\gamma d$ is about one thousandth. Note that d is the depth of the fluid layer and is in the order of minimeter. Since the flow motion is thermally driven, the Prandtl number is a measure of the sluggishness of the fluid velocity; higher Prandtl number implies slower motion and vice versa. On the other hand, in the absence of gravity the capillary number C is a measure of the surface deflection. And smaller C implies higher surface tension, which corresponds to a non-deflecting free surface. Discussions of the surface deflection effect as a function of C can be found in [6].

According to the above discussion, two assumptions are made in the present calculation: (1) the Prandtl number of the working fluid is large and therefore the Stokes equations are used instead of the full Navier–Stokes equations; and (2) the capillary number is small and the free surfaces of the MB rolls are flat. As a result, the following equations are solved for the MB convection:

$$\nabla \cdot V = 0\,, \tag{1}$$

$$\frac{\nabla p}{\rho} + \nu \nabla^2 V = 0\,, \tag{2}$$

$$\frac{\partial T}{\partial t} + (V \cdot \nabla) T = \kappa \nabla^2 T\,, \tag{3}$$

where $V = (u, v, w)^{\mathrm{T}}$ is the velocity vector, p is pressure, ρ in the density of the fluid, and T is temperature. The transport properties κ and ν and the density ρ are assumed constant in the flow field. Eq. (1) is the continuity equation, (2) is the Stokes equations for momentum conservation, and (3) is the energy equation.

To proceed, the governing equations are reduced to a first-order system by introducing new variables:

$$\boldsymbol{\Omega} = (\xi, \eta, \zeta)^{\mathrm{T}} = \nabla \times V\,, \tag{4}$$

$$Q = (q_x, q_y, q_z)^{\mathrm{T}} = \kappa \nabla T\,, \tag{5}$$

where $\boldsymbol{\Omega}$ is the vorticity with ξ, η, and ζ as the three components, and Q is the heat conduction flux vector with q_x, q_y, and q_z as the components in the respective directions. This step is necessary for the application of the LSFEM so that the C^0 elements can be used in the calculations. As a result, we obtain the following first-order flow equations:

$$\nabla \cdot V = 0\,, \tag{6}$$

$$\frac{\nabla p}{\rho} + \nu \nabla \times \boldsymbol{\Omega} = 0\,, \tag{7}$$

$$\frac{\partial T}{\partial t} + (V \cdot \nabla) T = \nabla \cdot Q\,. \tag{8}$$

Table 1
Properties of the silicon oil at 25 °C

Symbol	Property	Unit	Value
ν	Viscosity	cm^2/s	1.0
ρ	Density	g/cm^3	0.968
κ	Thermal diffusivity	cm^2/s	0.001095
γ	Surface tension coefficient	dyne/cm	13.96

In addition, the vorticity is divergence free, and heat conduction flux vector is curl free. That is

$$\nabla \cdot \boldsymbol{\Omega} = 0\,, \tag{9}$$

$$\nabla \times \boldsymbol{Q} = \mathbf{0}\,. \tag{10}$$

The boundary conditions on the bottom and the side walls of the container is the no-slip condition for velocities and vorticities,

$$u = v = w = 0$$
$$\boldsymbol{\Omega} \cdot \boldsymbol{n} = 0$$

where $\boldsymbol{n}$ is a unit vector normal to the wall. In addition, prescribed temperature at the heated bottom, and the insulated condition on the side walls are applied,

$$T = T_h\,, \quad \text{on the bottom;}$$
$$\boldsymbol{Q} \cdot \boldsymbol{n} = 0\,, \quad \text{on the vertical walls.}$$

On the free surface, the Marangoni boundary conditions are applied.

$$\rho\nu \frac{\partial u}{\partial z} = -\gamma \frac{\partial T}{\partial x}\,, \tag{11}$$

$$\rho\nu \frac{\partial v}{\partial z} = -\gamma \frac{\partial T}{\partial y}\,, \tag{12}$$

where γ is the surface tension coefficient. Note that the x and y coordinates are tangential to the free surface, and z is perpendicular to the free surface. By using the vorticities and heat conduction fluxes, the Marangoni conditions can also be expressed as

$$\rho\nu\eta = -\frac{\gamma}{\kappa} q_x\,, \tag{13}$$

$$\rho\nu\xi = \frac{\gamma}{\kappa} q_y\,, \tag{14}$$

Since a flat free surface is assumed, we also set $w = 0$ on the free surface.

The Marangoni conditions represent the relationship between the flow shear stress and the tangential surface tension force across the free surface. Any inhomogeneity of the surface tension (due to temperature variations) creates a shear force on the free surface and therefore results in flow motion. Therefore, the Marangoni conditions are the driving force of the MB convection. Mathematically, as boundary conditions, the Marangoni conditions are responsible for the strong coupling between the momentum equations and the energy equation. This is the difference between simulating the MB convection and simulating the RB convection, in which the energy equation is passively coupled with the momentum equations through a source term in the momentum equations.

The heat loss on the free surface is modeled by the usual heat transfer condition:

$$\rho\kappa C_p \frac{\partial T}{\partial z} = -h(T - T_c) \tag{15}$$

where h is a heat transfer coefficient, C_p is the constant pressure specific heat, and T_c is the prescribed cold temperature of the ambient air. The heat transfer mechanism on the free surface could be conduction, convection, radiation, and combinations of these effects.

2.2. Non-dimensionalization

Before the non-dimensionalization, the energy equation is reformulated in terms of the temperature perturbation θ, where

$$\theta = T - T_{\text{ave}}\,. \tag{16}$$

A linear distribution of the average temperature T_{ave} in the vertical direction is assumed, i.e.

$$T_{ave}(z) = T_h - \frac{z}{d}(T_h - T_c), \tag{17}$$

where T_h and T_c are the prescribed hot and cold temperatures to set up the MB instability, and d is the depth of the liquid layer. This procedure for the energy equation is commonly employed in the stability analyses of the MB flows. As a result, we obtain the following energy equation,

$$\frac{\partial\theta}{\partial t} + (\boldsymbol{V}\cdot\nabla)\theta - \frac{w\,\Delta T}{d} = \nabla\cdot\boldsymbol{Q}, \tag{18}$$

where w is the vertical component of the velocity, and $\Delta T = T_h - T_c$. Note that here we have redefined the heat conduction flux vector $\boldsymbol{Q}$ as the gradient of the temperature fluctuation, i.e. $\boldsymbol{Q} = \kappa\nabla\theta$.

The governing equations and the boundary conditions are then non-dimensionalized by the appropriate parameters. Here, we choose d and d^2/κ as the spatial and temporal scales. Therefore, the velocity scale is κ/d. In addition, the temperature variation θ is non-dimensionalized by ΔT.

$$u^* = \frac{ud}{\kappa}, \quad v^* = \frac{vd}{\kappa}, \quad w^* = \frac{wd}{\kappa},$$

$$\xi^* = \frac{\xi d^2}{\kappa}, \quad \eta^* = \frac{\eta d^2}{\kappa}, \quad \zeta^* = \frac{\zeta d^2}{\kappa},$$

$$p^* = \frac{pd}{\rho\nu\kappa}, \quad x^* = \frac{x}{d}, \quad y^* = \frac{y}{d},$$

$$z^* = \frac{z}{d}, \quad q_x^* = \frac{q_x d}{\kappa\,\Delta T}, \quad q_y^* = \frac{q_y d}{\kappa\,\Delta T},$$

$$q_z^* = \frac{q_z d}{\kappa\,\Delta T}, \quad \theta^* = \frac{\theta}{\Delta T},$$

Note that p^* is not dimensionless; p^* could be interpreted as a dimensionless pressure multiplied by a dimensional constant. This treatment is a common practice for the Stokes equation. As a result, the non-dimensionalized flow equations are

$$\nabla\cdot\boldsymbol{V} = 0, \tag{19}$$

$$\nabla p + \nabla\times\boldsymbol{\Omega} = 0, \tag{20}$$

$$\frac{\partial\theta}{\partial t} + (\boldsymbol{V}\cdot\nabla)\theta - w = \nabla\cdot\boldsymbol{Q}, \tag{21}$$

$$\nabla\cdot\boldsymbol{\Omega} = 0, \tag{22}$$

$$\nabla\times\boldsymbol{Q} = \boldsymbol{0}, \tag{23}$$

$$\nabla\times\boldsymbol{V} = \boldsymbol{\Omega}, \tag{24}$$

$$\nabla\theta = \boldsymbol{Q}. \tag{25}$$

Note that, the superscript $*$ has been dropped for convenience.

The Marangoni boundary conditions are also non-dimensionalized by the spatial and temporal scales, and we get

$$\eta = -M_a q_x, \tag{26}$$

$$\xi = M_a q_y, \tag{27}$$

where

$$M_a = \frac{\gamma\,\Delta T\,d}{\rho\nu\kappa} \tag{28}$$

is the Marangoni number.

Similarly, after the non-dimensionalization the heat convection condition on the free surface becomes,

$$q_z + B_i\theta = 0 \tag{29}$$

where $B_i = hd/\kappa\rho C_p$ is the Biot number, which is a dimensionless measure of the heat loss on the free surface. Usually, the ambient environment is well controlled in the MB experiments and the heat transfer on the fluid surface is not efficient. Furthermore, we note that the energy equation and its boundary conditions are formulated in terms of the temperature variation θ instead of temperature itself. Therefore, it is a reasonable assumption to let $B_i = 0$, which implies that the heat transfer to the ambient air through the temperature fluctuation θ on the free surface is negligible. Instead, all heat transfer on the free surface is through the gradient of the average temperature T_{ave}. As a result, the boundary condition for the energy equation on the free surface becomes $q_z = 0$.

2.3. Div–curl–grad formulation

First, we apply the first-order backward differencing to the temporal derivative term of the energy equation. In addition, by using the definition of the heat conduction fluxes, we transform the nonlinear convective terms of the energy equation $\boldsymbol{V}\cdot\nabla\theta$ into an algebraic expression $\boldsymbol{V}\cdot\boldsymbol{Q}$. As a result, a new set of first-order equations is obtained:

$$\nabla\cdot\boldsymbol{V} = 0\,, \tag{30}$$

$$\nabla\times\boldsymbol{V} = \boldsymbol{\Omega}\,, \tag{31}$$

$$\nabla\cdot\boldsymbol{\Omega} = 0\,, \tag{32}$$

$$\nabla\times\boldsymbol{\Omega} + \nabla p = \boldsymbol{0}\,, \tag{33}$$

$$\nabla\cdot\boldsymbol{Q} = \frac{1}{\Delta t}(\theta - \theta^{n-1}) + \boldsymbol{V}\cdot\boldsymbol{Q} - w\,, \tag{34}$$

$$\nabla\times\boldsymbol{Q} = 0\,, \tag{35}$$

$$\nabla\theta = \boldsymbol{Q}\,, \tag{36}$$

where Δt is the time step, and the superscript $n-1$ denotes the previous time step. Note that all right-hand sides are algebraic and they have nothing to do with the classification of this equation set. The left-hand sides are composed of div–curl–grad operations and they are responsible for the characteristics of the partial differential equations. In terms of components, we have arrived at a system of fifteen equations and eleven unknowns. Seemingly, we have an 'over-determined' problem on our hands.

2.4. Ellipticity

Usually, a system of first-order partial differential equations are elliptic if the number of equations and unknowns are even such that complex conjugate eigenvalues can be obtained as the roots of the characteristic polynomial of the equation set. Apparently, Eqs. (30)–(36) cannot be fitted into this paradigm. To overcome the difficulty, dummy variables and additional equations associated with the dummy variables are introduced into the governing equations to reconstruct an even-number unknowns/equations system.

Apparently, Eqs. (30)–(36) are composed of three div–curl–grad systems: (30) and (31) are a div–curl system for velocities; (32) and (33) are a div–curl system for vorticity and pressure; and (34), (35) and (36) are a div–curl–grad system for the heat fluxes and temperature fluctuation. In the first system, (30) and (31), the div and curl operators operate on three unknowns, u, v and w, and the system is composed of four equations. Here, we introduce a new variable ϕ, and the system becomes

$$\nabla\cdot\boldsymbol{V} = 0\,, \tag{37}$$

$$\nabla\phi + \nabla\times\boldsymbol{V} = \boldsymbol{\Omega}\,, \tag{38}$$

where the dummy variable ϕ satisfies the boundary condition $\phi = 0$ on Γ. By applying the divergence operator to (38) and considering $\nabla \cdot \nabla \times \boldsymbol{V} = 0$ and $\nabla \cdot \boldsymbol{\Omega} = 0$ we have

$$\nabla^2 \phi = 0 \quad \text{in } \Omega, \tag{39}$$

$$\phi = 0 \quad \text{on } \Gamma. \tag{40}$$

Therefore, a trivial solution $\phi \equiv 0$ is obtained, and the original system has not been changed.

The second div–curl set, (32) and (33), is constructed by four equations and four unknowns i.e. ξ, η, ζ and p, operated by the div and curl operators, and no dummy variable is needed.

The third div–curl–grad set, (34)–(36), has four unknowns (θ, q_x, q_y and q_z) determined by seven equations. Hence, four dummy variables and one equation are introduced into this system:

$$\nabla \cdot \boldsymbol{Q} = f, \tag{41}$$

$$\nabla \vartheta + \nabla \times \boldsymbol{Q} = 0, \tag{42}$$

$$\nabla \cdot \boldsymbol{\Psi} = 0, \tag{43}$$

$$\nabla \times \boldsymbol{\Psi} + \nabla \theta = \boldsymbol{Q}, \tag{44}$$

where ϑ and $\boldsymbol{\Psi} = (\psi_1, \psi_2, \psi_3)$ are the dummy variables, and f is the right-hand side of the energy equation (see Eq. (34)). As such, this subsystem has eight unknowns and eight equations. By applying a divergence operator to (42) and considering $\nabla \cdot \nabla \times \boldsymbol{Q} = 0$, we have $\nabla^2 \vartheta = 0$ inside the computational domain. Combined with the prescribed boundary condition $\vartheta = 0$ at Γ, we get $\vartheta \equiv 0$, and the introduction of ϑ does not change the original equations. Similarly, by applying a curl to (44), and considering $\nabla \times \nabla \theta = \nabla \times \boldsymbol{Q} = \boldsymbol{0}$, we have

$$\nabla \times (\nabla \times \boldsymbol{\Psi}) = 0. \tag{45}$$

We also know that

$$\nabla \cdot (\nabla \times \boldsymbol{\Psi}) = 0. \tag{46}$$

With the boundary condition $\boldsymbol{n} \times \boldsymbol{\Psi} = 0$, it can be shown that $\boldsymbol{\Psi} \equiv \boldsymbol{0}$. Therefore, the introduction of $\boldsymbol{\Psi}$ does not change the original system of equations.

Facilitated by the dummy variables, we now have sixteen equations and sixteen unknowns. In the Cartesian coordinates, the first-order system of equations have the following form:

$$\frac{\partial u}{\partial x} + \frac{\partial v}{\partial y} + \frac{\partial w}{\partial z} = 0, \tag{47}$$

$$\frac{\partial \phi}{\partial x} + \frac{\partial w}{\partial y} - \frac{\partial v}{\partial z} = \xi, \tag{48}$$

$$\frac{\partial \phi}{\partial y} + \frac{\partial u}{\partial z} - \frac{\partial w}{\partial x} = \eta, \tag{49}$$

$$\frac{\partial \phi}{\partial z} + \frac{\partial v}{\partial x} - \frac{\partial u}{\partial y} = \zeta, \tag{50}$$

$$\frac{\partial \xi}{\partial x} + \frac{\partial \eta}{\partial y} + \frac{\partial \zeta}{\partial z} = 0, \tag{51}$$

$$\frac{\partial \zeta}{\partial y} - \frac{\partial \eta}{\partial z} + \frac{\partial p}{\partial x} = 0, \tag{52}$$

$$\frac{\partial \xi}{\partial z} - \frac{\partial \zeta}{\partial x} + \frac{\partial p}{\partial y} = 0, \tag{53}$$

$$\frac{\partial \eta}{\partial x} - \frac{\partial \xi}{\partial y} + \frac{\partial p}{\partial z} = 0, \tag{54}$$

$$\frac{\partial q_x}{\partial x}+\frac{\partial q_y}{\partial y}+\frac{\partial q_z}{\partial z}=f\,, \tag{55}$$

$$\frac{\partial \vartheta}{\partial x}+\frac{\partial q_z}{\partial y}-\frac{\partial q_y}{\partial z}=0\,, \tag{56}$$

$$\frac{\partial \vartheta}{\partial y}+\frac{\partial q_x}{\partial z}-\frac{\partial q_z}{\partial x}=0\,, \tag{57}$$

$$\frac{\partial \vartheta}{\partial z}+\frac{\partial q_y}{\partial x}-\frac{\partial q_x}{\partial y}=0\,, \tag{58}$$

$$\frac{\partial \psi_1}{\partial x}+\frac{\partial \psi_2}{\partial y}+\frac{\partial \psi_3}{\partial z}=0\,, \tag{59}$$

$$\frac{\partial \theta}{\partial x}+\frac{\partial \psi_3}{\partial y}-\frac{\partial \psi_2}{\partial z}=q_x\,, \tag{60}$$

$$\frac{\partial \theta}{\partial y}+\frac{\partial \psi_1}{\partial z}-\frac{\partial \psi_3}{\partial x}=q_y\,, \tag{61}$$

$$\frac{\partial \theta}{\partial z}+\frac{\partial \psi_2}{\partial x}-\frac{\partial \psi_1}{\partial y}=q_z\,, \tag{62}$$

We then cast the equation set into a matrix form:

$$\boldsymbol{A}_1\frac{\partial \boldsymbol{q}}{\partial x}+\boldsymbol{A}_2\frac{\partial \boldsymbol{q}}{\partial y}+\boldsymbol{A}_3\frac{\partial \boldsymbol{q}}{\partial z}=\boldsymbol{S}\,, \tag{63}$$

in which the unknown vector $\boldsymbol{q}$ is defined as

$$\boldsymbol{q}=(u, v, w, \phi, \xi, \eta, \zeta, p, q_x, q_y, q_z, \vartheta, \psi_1, \psi_2, \psi_3, T)^{\mathrm{T}}\,, \tag{64}$$

and $\boldsymbol{S}$ represents the algebraic terms in the right-hand side of the equations.

The coefficient matrices $\boldsymbol{A}_1$, $\boldsymbol{A}_2$ and $\boldsymbol{A}_3$ are

$$\boldsymbol{A}_1=\begin{pmatrix}
1&0&0&0&0&0&0&0&0&0&0&0&0&0&0&0\\
0&0&0&1&0&0&0&0&0&0&0&0&0&0&0&0\\
0&0&-1&0&0&0&0&0&0&0&0&0&0&0&0&0\\
0&1&0&0&0&0&0&0&0&0&0&0&0&0&0&0\\
0&0&0&0&1&0&0&0&0&0&0&0&0&0&0&0\\
0&0&0&0&0&0&0&1&0&0&0&0&0&0&0&0\\
0&0&0&0&0&0&-1&0&0&0&0&0&0&0&0&0\\
0&0&0&0&0&1&0&0&0&0&0&0&0&0&0&0\\
0&0&0&0&0&0&0&0&1&0&0&0&0&0&0&0\\
0&0&0&0&0&0&0&0&0&0&0&1&0&0&0&0\\
0&0&0&0&0&0&0&0&0&0&-1&0&0&0&0&0\\
0&0&0&0&0&0&0&0&0&1&0&0&0&0&0&0\\
0&0&0&0&0&0&0&0&0&0&0&0&1&0&0&0\\
0&0&0&0&0&0&0&0&0&0&0&0&0&1&0&0\\
0&0&0&0&0&0&0&0&0&0&0&0&0&0&-1&0\\
0&0&0&0&0&0&0&0&0&0&0&0&0&1&0&0
\end{pmatrix} \tag{65}$$

$$A_2 = \begin{pmatrix}
0 & 1 & 0 & 0 & 0 & 0 & 0 & 0 & 0 & 0 & 0 & 0 & 0 & 0 & 0 & 0 \\
0 & 0 & 1 & 0 & 0 & 0 & 0 & 0 & 0 & 0 & 0 & 0 & 0 & 0 & 0 & 0 \\
0 & 0 & 0 & 1 & 0 & 0 & 0 & 0 & 0 & 0 & 0 & 0 & 0 & 0 & 0 & 0 \\
-1 & 0 & 0 & 0 & 0 & 0 & 0 & 0 & 0 & 0 & 0 & 0 & 0 & 0 & 0 & 0 \\
0 & 0 & 0 & 0 & 0 & 1 & 0 & 0 & 0 & 0 & 0 & 0 & 0 & 0 & 0 & 0 \\
0 & 0 & 0 & 0 & 0 & 0 & 1 & 0 & 0 & 0 & 0 & 0 & 0 & 0 & 0 & 0 \\
0 & 0 & 0 & 0 & 0 & 0 & 0 & 1 & 0 & 0 & 0 & 0 & 0 & 0 & 0 & 0 \\
0 & 0 & 0 & 0 & -1 & 0 & 0 & 0 & 0 & 0 & 0 & 0 & 0 & 0 & 0 & 0 \\
0 & 0 & 0 & 0 & 0 & 0 & 0 & 0 & 0 & 1 & 0 & 0 & 0 & 0 & 0 & 0 \\
0 & 0 & 0 & 0 & 0 & 0 & 0 & 0 & 0 & 0 & 1 & 0 & 0 & 0 & 0 & 0 \\
0 & 0 & 0 & 0 & 0 & 0 & 0 & 0 & 0 & 0 & 0 & 1 & 0 & 0 & 0 & 0 \\
0 & 0 & 0 & 0 & 0 & 0 & 0 & 0 & -1 & 0 & 0 & 0 & 0 & 0 & 0 & 0 \\
0 & 0 & 0 & 0 & 0 & 0 & 0 & 0 & 0 & 0 & 0 & 0 & 0 & 1 & 0 & 0 \\
0 & 0 & 0 & 0 & 0 & 0 & 0 & 0 & 0 & 0 & 0 & 0 & 0 & 0 & 1 & 0 \\
0 & 0 & 0 & 0 & 0 & 0 & 0 & 0 & 0 & 0 & 0 & 0 & 0 & 0 & 0 & 1 \\
0 & 0 & 0 & 0 & 0 & 0 & 0 & 0 & 0 & 0 & 0 & 0 & -1 & 0 & 0 & 0
\end{pmatrix} \tag{66}$$

$$A_3 = \begin{pmatrix}
0 & 0 & 1 & 0 & 0 & 0 & 0 & 0 & 0 & 0 & 0 & 0 & 0 & 0 & 0 & 0 \\
0 & -1 & 0 & 0 & 0 & 0 & 0 & 0 & 0 & 0 & 0 & 0 & 0 & 0 & 0 & 0 \\
1 & 0 & 0 & 0 & 0 & 0 & 0 & 0 & 0 & 0 & 0 & 0 & 0 & 0 & 0 & 0 \\
0 & 0 & 0 & 1 & 0 & 0 & 0 & 0 & 0 & 0 & 0 & 0 & 0 & 0 & 0 & 0 \\
0 & 0 & 0 & 0 & 0 & 0 & 1 & 0 & 0 & 0 & 0 & 0 & 0 & 0 & 0 & 0 \\
0 & 0 & 0 & 0 & 0 & -1 & 0 & 0 & 0 & 0 & 0 & 0 & 0 & 0 & 0 & 0 \\
0 & 0 & 0 & 0 & 1 & 0 & 0 & 0 & 0 & 0 & 0 & 0 & 0 & 0 & 0 & 0 \\
0 & 0 & 0 & 0 & 0 & 0 & 0 & 1 & 0 & 0 & 0 & 0 & 0 & 0 & 0 & 0 \\
0 & 0 & 0 & 0 & 0 & 0 & 0 & 0 & 0 & 1 & 0 & 0 & 0 & 0 & 0 & 0 \\
0 & 0 & 0 & 0 & 0 & 0 & 0 & 0 & -1 & 0 & 0 & 0 & 0 & 0 & 0 & 0 \\
0 & 0 & 0 & 0 & 0 & 0 & 0 & 1 & 0 & 0 & 0 & 0 & 0 & 0 & 0 & 0 \\
0 & 0 & 0 & 0 & 0 & 0 & 0 & 0 & 0 & 0 & 1 & 0 & 0 & 0 & 0 & 0 \\
0 & 0 & 0 & 0 & 0 & 0 & 0 & 0 & 0 & 0 & 0 & 0 & 0 & 1 & 0 & 0 \\
0 & 0 & 0 & 0 & 0 & 0 & 0 & 0 & 0 & 0 & 0 & 0 & -1 & 0 & 0 & 0 \\
0 & 0 & 0 & 0 & 0 & 0 & 0 & 0 & 0 & 0 & 0 & 1 & 0 & 0 & 0 & 0 \\
0 & 0 & 0 & 0 & 0 & 0 & 0 & 0 & 0 & 0 & 0 & 0 & 0 & 0 & 1 & 0
\end{pmatrix} \tag{67}$$

The characteristic polynomial of the system is

$$\det(\boldsymbol{A}_1\lambda_1 + \boldsymbol{A}_2\lambda_2 + \boldsymbol{A}_3\lambda_3) = 0\,, \tag{68}$$

The roots of the equation determine the type of the differential equation set. The left-hand side of (68) can be written as

$$\begin{aligned}
\det\begin{pmatrix} \boldsymbol{C} & 0 & 0 & 0 \\ 0 & \boldsymbol{C} & 0 & 0 \\ 0 & 0 & \boldsymbol{C} & 0 \\ 0 & 0 & 0 & \boldsymbol{C} \end{pmatrix} &= (\det \boldsymbol{C})^4 \\
&= \det\begin{pmatrix} \lambda_1 & \lambda_2 & \lambda_3 & 0 \\ 0 & -\lambda_3 & \lambda_2 & \lambda_1 \\ \lambda_3 & 0 & -\lambda_1 & \lambda_2 \\ -\lambda_2 & \lambda_1 & 0 & \lambda_3 \end{pmatrix}^4 \\
&= (\lambda_1^2 + \lambda_2^2 + \lambda_3^2)^8
\end{aligned} \tag{69}$$

Eq. (69) cannot be equal to zero for distinct real roots of λ_1, λ_2 and λ_3, and the equation set is indeed elliptic.

2.5. Boundary conditions

Because the number of equations is even and the equation set is elliptic, the required boundary conditions are standard. In addition, the equation set is first-order, and only Dirichlet boundary conditions are used. Facilitated

Table 2
Boundary conditions

Conditions	Flow equations	Heat equations
Heated bottom	$u = v = w = 0$	$\theta = 0$, $Q_{\tau 1} = Q_{\tau 2} = 0$
	$\boldsymbol{n} \cdot \boldsymbol{\Omega} = 0$	$(\vartheta = 0)$
Insulated walls	$u = v = w = 0$	$\boldsymbol{Q} \cdot \boldsymbol{n} = 0$, $(\boldsymbol{n} \times \boldsymbol{\Psi} = \boldsymbol{0})$
	$(\phi = 0)$	
Free surface	$\boldsymbol{n} \cdot \boldsymbol{V} = 0$, $\Omega_{\tau 1} = M_a Q_{\tau 2}^{n-1}$	$\boldsymbol{Q} \cdot \boldsymbol{n} = 0$, $(\boldsymbol{n} \times \boldsymbol{\Psi} = 0)$
	$\Omega_{\tau 2} = -M_a Q_{\tau 1}^{n-1} (\phi = 0)$	

by the dummy variables, we have sixteen unknowns governed by sixteen equations. As such, eight boundary conditions are required on each boundary. For the purpose of discussion, we divide the system of equations into two groups: the flow equations, and the heat equations. On each boundary, four boundary conditions are required for each group. In Table 2, we propose the permissible boundary conditions for the MB convection.

The outward normal vector of the boundary is denoted by $\boldsymbol{n}$, and the tangential unit vector is $\tau = (\tau_1, \tau_2)$ with τ_1 and τ_2 as the two orthogonal components. When used as a subscript, τ_1 and τ_2 denote the two mutually orthogonal components of a tangential vector. For example, $\boldsymbol{Q}_{\tau 1}$ and $\boldsymbol{Q}_{\tau 2}$ denote the two tangential components of $\boldsymbol{Q}$ on the heated bottom.

For a typical MB flow, there are three type boundary conditions: (1) the heated bottom wall condition, (2) the insulated vertical wall condition, and (3) the free surface condition. For each type boundary, we enforce the known boundary conditions as listed in Section 2.1. In addition, we invoke the pseudo-boundary conditions of the dummy variables to complement the system. For this reason, these null boundary conditions are put in parentheses. For the Marangoni conditions on the free surface, we specify the vorticities by using the heat conduction fluxes tangential to the free surface from the previous time step. This treatment is in accordance with the flow physics that the flow motion is driven by the uneven distribution of the surface temperature. Therefore, fore each time step, the semi-discretized governing equations (63) are elliptic and their boundary conditions are illustrated.

3. The least-squares finite element method

The LSFEM is used to solve the first-order equations (63). The right-hand side vector $\boldsymbol{S}$ of (63) is an algebraic expression of dependent variables to be solved, i.e.

$$s_i = s_i(q_1, q_2, \ldots, q_{16}) \quad i = 1, 2, \ldots, 16 \tag{70}$$

where q_j, $j = 1, \ldots, 16$ are the dependent variables. The nonlinear terms are linearized by Newton's method in the following fashion:

$$s_i^{m+1} = s_i^m + \sum_{j=1}^{16} \left(\frac{\partial s_i}{\partial q_j} \right)^m \Delta q_j \,, \tag{71}$$

where the superscript m denotes the previous Newton's method step and $m + 1$ is the current step. $\Delta q_j = q_j^{m+1} - q_j^m$ is the increment of the flow variables in each Newton's iteration. After manipulation, we obtain a new set of equations in vector form ready for finite-element discretization,

$$\boldsymbol{A}_0^m \Delta \boldsymbol{q} + \boldsymbol{A}_1^m \frac{\partial \Delta \boldsymbol{q}}{\partial x} + \boldsymbol{A}_1^m \frac{\partial \boldsymbol{q}^m}{\partial x} + \boldsymbol{A}_2^m \frac{\partial \Delta \boldsymbol{q}}{\partial y} + \boldsymbol{A}_2^m \frac{\partial \boldsymbol{q}^m}{\partial y} + \boldsymbol{A}_3^m \frac{\partial \Delta \boldsymbol{q}}{\partial z} + \boldsymbol{A}_3^m \frac{\partial \boldsymbol{q}^m}{\partial z} + \boldsymbol{S}^m = 0 \,. \tag{72}$$

To proceed, the governing equations are cast into the following operator form:

$$L \, \Delta q = f \,, \tag{73}$$

where the linear operator $\boldsymbol{L}$ is defined as

$$\boldsymbol{L} = \boldsymbol{A}_0^m + \boldsymbol{A}_1^m \frac{\partial}{\partial x} + \boldsymbol{A}_2^m \frac{\partial}{\partial y} + \boldsymbol{A}_3^m \frac{\partial}{\partial z}. \tag{74}$$

The right-hand side vector is

$$\boldsymbol{f} = -\boldsymbol{A}_1^m \frac{\partial \boldsymbol{q}^m}{\partial x} - \boldsymbol{A}_2^m \frac{\partial \boldsymbol{q}^m}{\partial y} - \boldsymbol{A}_3^m \frac{\partial \boldsymbol{q}^m}{\partial z} - \boldsymbol{S}^m. \tag{75}$$

We then define the least-squares functional of the residual $\boldsymbol{R} = \boldsymbol{L}\,\Delta\boldsymbol{q} - \boldsymbol{f}$ for admissible $\Delta\boldsymbol{q}$ as

$$J(\Delta\boldsymbol{q}) = \int_\Omega \boldsymbol{R}^{\mathrm{T}} \cdot \boldsymbol{R}\, \mathrm{d}\Omega. \tag{76}$$

Minimizing the least-squares functional $J(\Delta\boldsymbol{q})$ with respect to $\Delta\boldsymbol{q}$ leads to

$$\delta J(\Delta\boldsymbol{q}) = 0. \tag{77}$$

That is

$$\int_\Omega (\boldsymbol{L}\,\delta\Delta\boldsymbol{q})^{\mathrm{T}} \cdot (\boldsymbol{L}\,\Delta\boldsymbol{q} - \boldsymbol{f})\, \mathrm{d}\Omega = 0, \tag{78}$$

where δ denotes the variation of the function. Let $\delta\Delta\boldsymbol{q} = \boldsymbol{v}$, and (78) can be written as

$$\int_\Omega (\boldsymbol{L}\boldsymbol{v})^{\mathrm{T}} (\boldsymbol{L}\,\Delta\boldsymbol{q})\, \mathrm{d}\Omega = \int_\Omega (\boldsymbol{L}\boldsymbol{v})^{\mathrm{T}} \boldsymbol{f}\, \mathrm{d}\Omega. \tag{79}$$

To employ the finite element method, the computational domain is decomposed into N_e elements and the element shape functions Φ_i's are introduced. The discretized solution in each element $\Delta\boldsymbol{q}_h^e(t, x, y, z)$ can be expressed as

$$\Delta\boldsymbol{q}_h^e(t, x, y, z) = \sum_{i=1}^{N_n} \Phi_i(x, y, z)(\Delta\boldsymbol{Q}_i(t))^e, \tag{80}$$

where N_n is the number of nodes per element and the $(\Delta\boldsymbol{Q}_i(t))^e$ are the nodal values of $\Delta\boldsymbol{q}$. The test function $\boldsymbol{v}$ is chosen as

$$\boldsymbol{v}(x, y, z) = \Phi_i(x, y, z)\boldsymbol{I}, \tag{81}$$

where $\boldsymbol{I}$ is the identity matrix. Substituting (80) and (81) into (79) gives the linear algebraic equation

$$\boldsymbol{K}^m\,\Delta\boldsymbol{Q} = \boldsymbol{F}^m, \tag{82}$$

where $\Delta\boldsymbol{Q}$ denotes the global nodal values of $\Delta\boldsymbol{q}(x, y)$, and the final global matrix is

$$\boldsymbol{K}^m = \sum_{e=1}^{N_e} (\boldsymbol{K}^m)^e \tag{83}$$

That is, the global matrix $\boldsymbol{K}^m$ is assembled from the element matrix $(\boldsymbol{K}^m)^e$, which is defined as

$$(\boldsymbol{K}_{ij}^m)^e = \int_{\Omega_e} (\boldsymbol{L}\Phi_i)^{\mathrm{T}} \cdot (\boldsymbol{L}\Phi_j)\, \mathrm{d}\Omega. \tag{84}$$

The final right-hand side vector $\boldsymbol{F}^m$ is assembled from the element vector $(\boldsymbol{F}_i^m)^e$, which is given as

$$(\boldsymbol{F}_i^m)^e = \int_{\Omega_e} (\boldsymbol{L}\Phi_i)^{\mathrm{T}} \cdot \boldsymbol{f}\, \mathrm{d}\Omega \tag{85}$$

An important feature of the least-squares finite element method can be observed in (79) and (84), i.e. the matrix is symmetric. In addition, as long as the solution exists, the global matrix is also positive-definite.

The JCG method [26] is employed to invert the coefficient matrix. The method is an efficient and straightforward approach for inverting a symmetric, positive-definite matrix. As long as the solution exists, the

numerical convergence of the JCG method is guaranteed. Because the Jacobi preconditioning procedure consists of modifying only the diagonal terms of the global matrix, the preconditioned global matrix does not suffer from any fill-in and the whole procedure can be implemented n an element-by-element fashion such that no global matrix need to be stored and fine-grain parallelization is straightforward. We consider this merit of the LSFEM specially attractive for large-scale calculations.

4. Results and discussions

The numerical results reported here are the simulated MB flow in square containers. The flow features of the MB convection depend on the aspect ratio of the containers (A_r) and the Marangoni number (M_a). A_r is defined as the ratio of the horizontal distance between the opposite walls to the depth of the liquid layer. As shown in Fig. 1, the configuration consists of four insulated vertical walls, a heated bottom surface, and a flat free surface. Fig. 1 also illustrates the specified boundary conditions.

In the present paper, we want to recapture the unusual MB planforms in small containers reported by Koschmieder and Prahl [3]. Here, four cases are reported: the two, three, four and five-cell MB convection. A mesh of $51 \times 51 \times 19$ is used. The mesh is uniform in the x and y directions, and is clustered near the free surface in the z direction. For different cases, the aspect ratio A_r are different and the mesh is adjusted accordingly. Although not shown, we have conducted the mesh refinement study for the four-cell case by doubling the mesh size in each coordinate direction. Essentially, we have obtained the same numerical solution.

There are three loops of iterations: (1) the outer loop is the time marching part; (2) the intermediate loop updates the coefficient matrices and source terms by Newton's method; and (3) the inner loop solves the variable increment Δq by inverting the global matrix using the JCG method. Typically, it takes about 50 to 100 time-marching steps to converge about four order of $q^n - q^{n-1}$, where n denotes the time step. Further convergence is generally much slower. After about 50 to 100 time steps, the numerical method usually has already caught the MB patterns. Within each time step, we perform Newton's method about three to five times

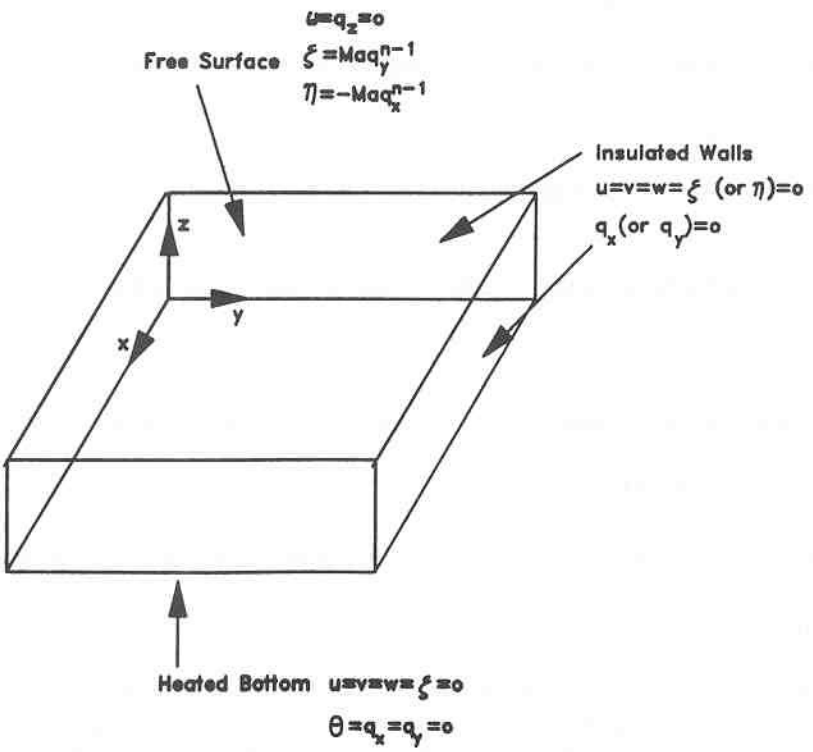

Fig. 1. A schematic of the computational domain.

to update the coefficient matrices and the source vector. For each Newton's step, it typically takes about 300 to 500 JCG steps to invert the coefficient matrix.

To start the calculation, we initialize the temperature field by the initial condition used in [16]:

$$\theta(x, y, z, 0) = \epsilon(x, y)z(2 - z) \tag{86}$$

The field $\epsilon(x, y)$ is the superposition of all Fourier modes supported by the employed numerical mesh. The magnitude of $\epsilon(x, y)$ is set to be one thousandth. All other flow properties are initialized by zeros. As time

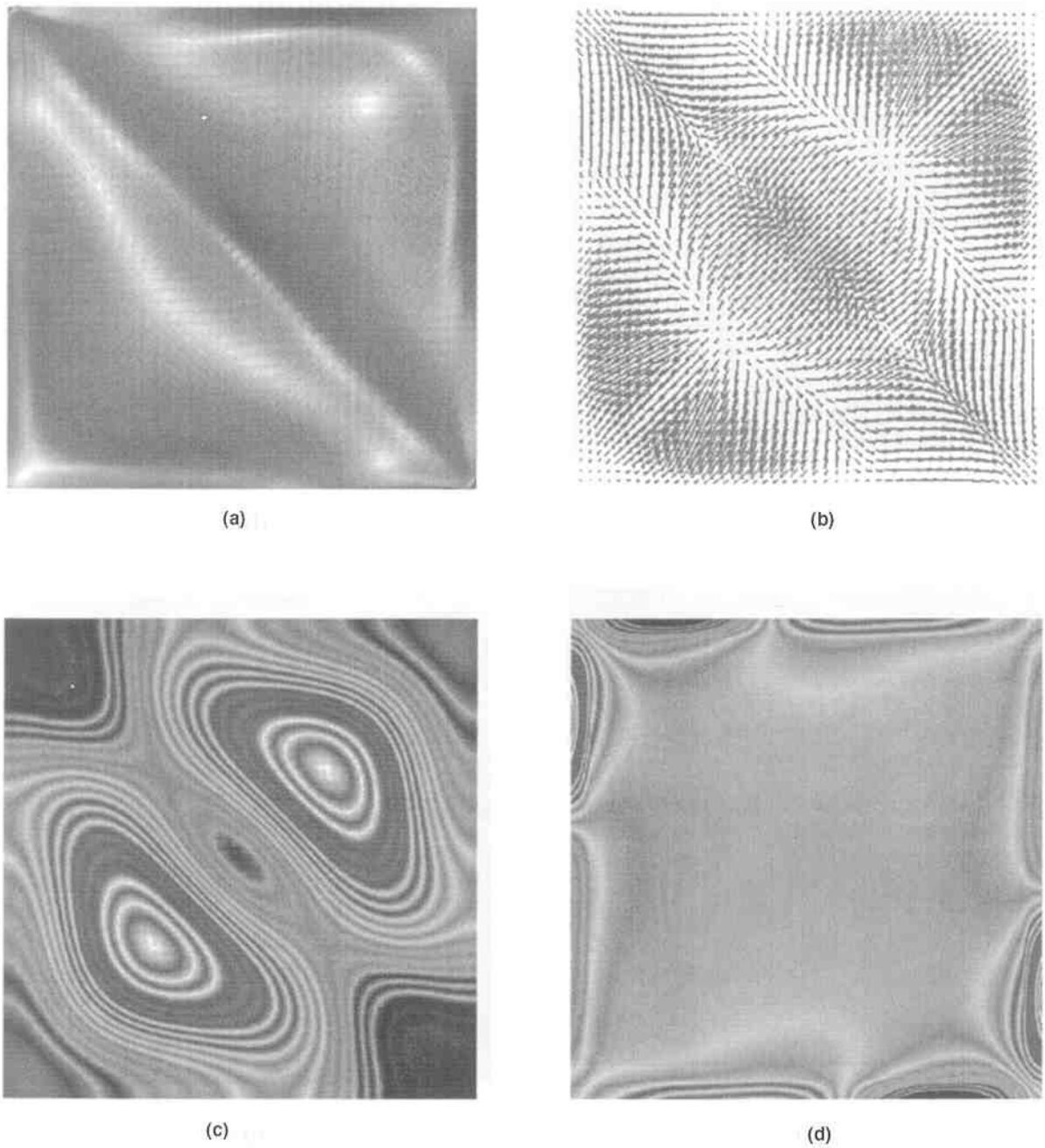

Fig. 2. The Marangoni–Benard convection in a square container with two cells for $M_a = 87$ and $A_r = 5.68$. (a) The pattern; (b) the velocity vectors on the free surface; (c) the temperature contours on the free surface; and (d) the vertical vorticity contours on the free surface.

evolves, the numerical procedure will pick up the most unstable mode and suppress others. In addition, we usually start our calculations with very low M_a and gradually increase the M_a until the onset of the flow convection. Gradually, the numerical calculations converge to the selected planforms.

Fig. 2 shows the numerical solution of a two-cell MB convection. Four plots are shown: (2a) the MB planforms; (2b) the velocity vectors on the free surface; (2c) the temperature contours on the free surface; and (2d) the contours of the vertical vorticity on the free surface. The planform (2a) shown here is actually the smoothed contour plot of the velocity profile just beneath the free surface. The surface topology represents the

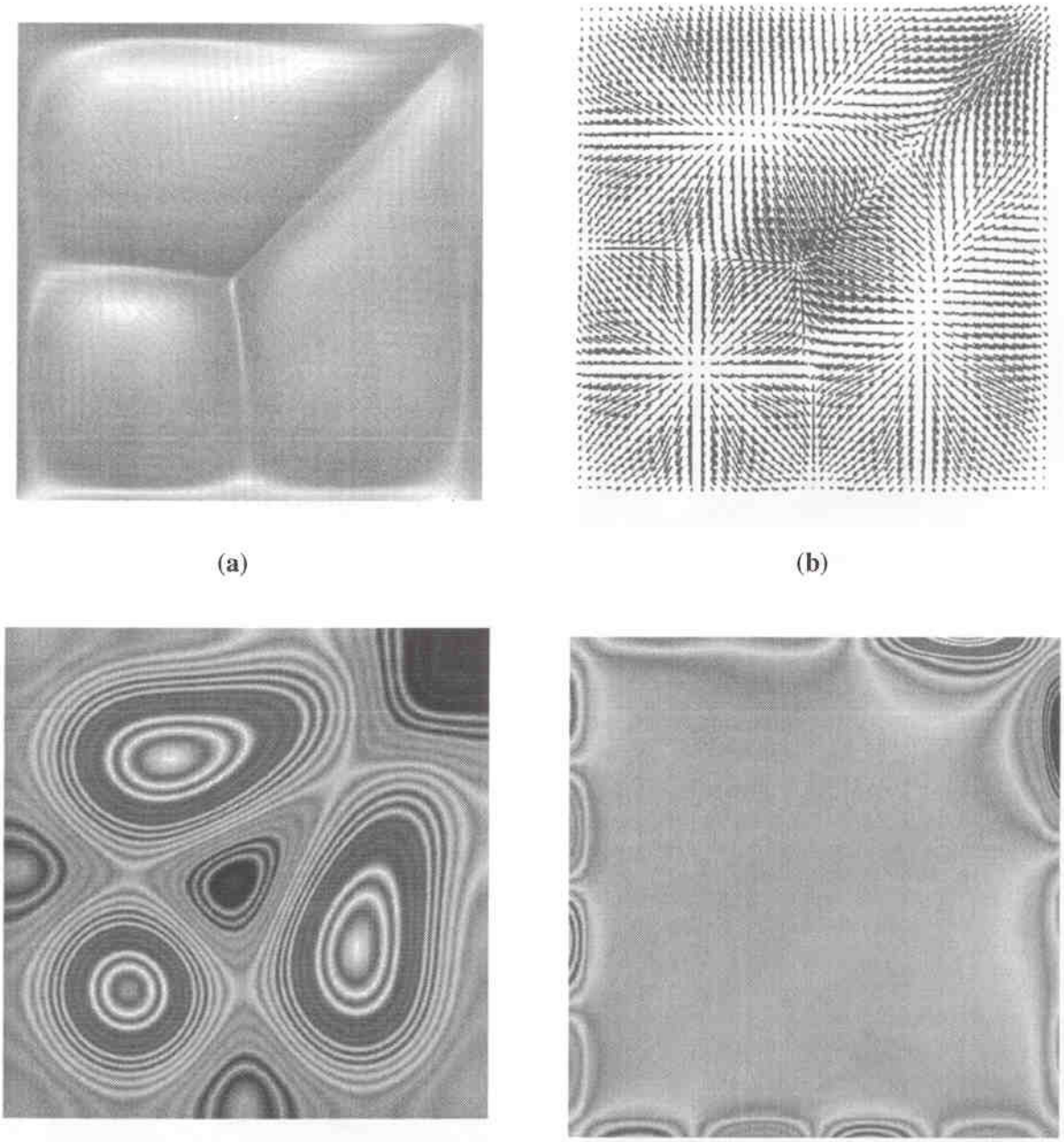

Fig. 3. The Marangoni–Benard convection in a square container with three cells for $M_a = 95$ and $A_r = 6.18$. (a) the pattern; (b) the velocity vectors on the free surface; (c) the temperature contours on the free surface; and (d) the vertical vorticity contours on the free surface.

velocity distribution: the bulge-up portions represent the rising flow motion and the valleys are the downward flow. For $M_a = 87$ and $A_r = 5.68$, two triangular MB cells are obtained. The simulated pattern is identical to that reported by Koschmieder et al. [3].

At the centers of the triangles, temperature is hotter and therefore the surface tension is smaller as compared to the area along the walls and the diagonal valley, where the temperature is colder. Accordingly, this unbalanced surface tension force results in flow motions from the hot region to the cold region; i.e. from the center of the MB cell to the cell boundary. To replenish the hot region, hot fluid is dragged up from the bottom of the container, and therefore the MB convection is sustained. As shown in Fig. (2c), the coldest spots on the free surface is the higher-left and lower-right corners, where the cold fluid is pushed downward to be heated up.

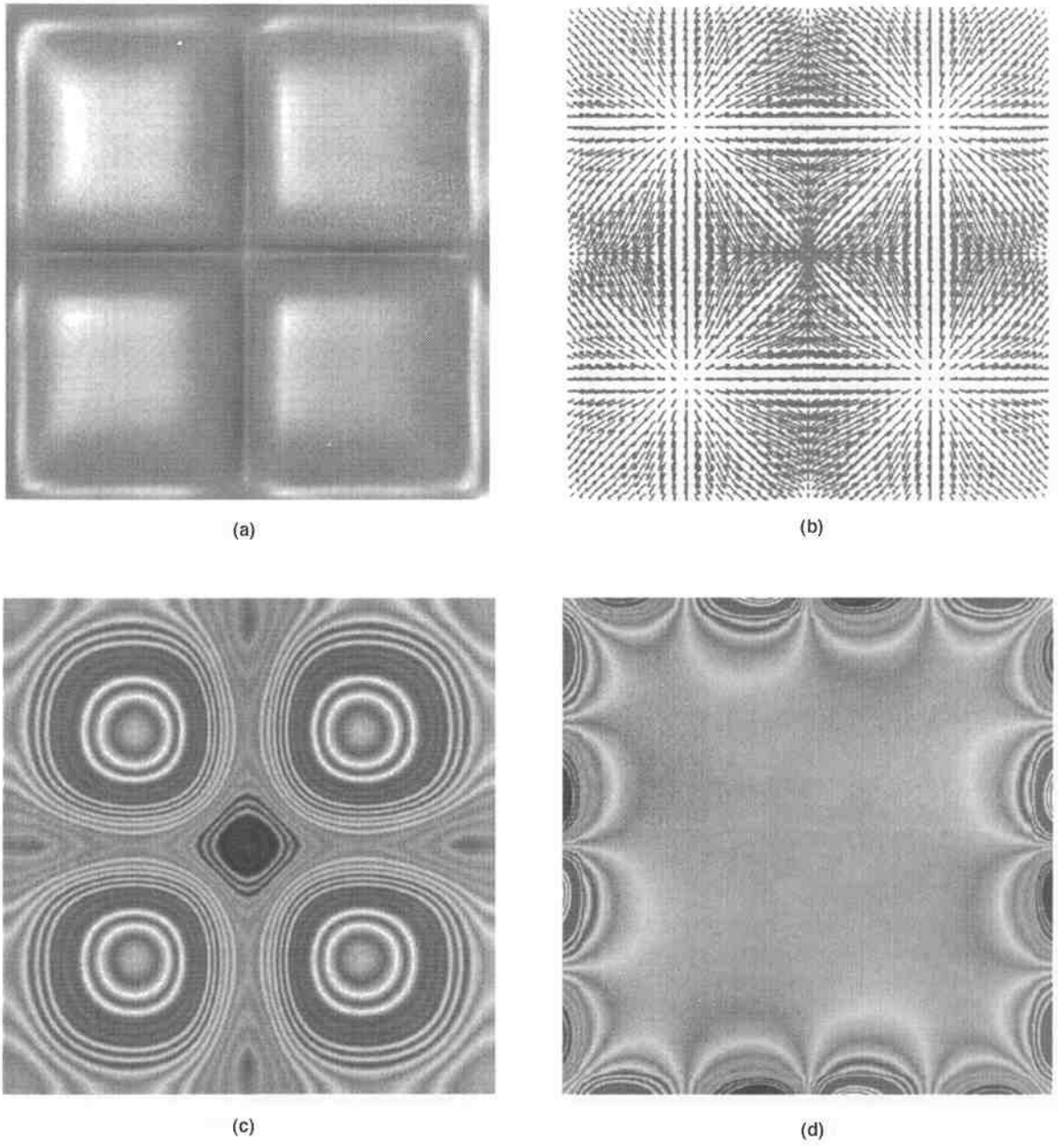

Fig. 4. The Marangoni–Benard convection in a square container with four cells for $M_a = 95$ and $A_r = 6.36$. (a) The pattern; (b) the velocity vectors on the free surface; (c) the temperature contours on the free surface; and (d) the vertical vorticity contours on the free surface.

It is interesting to note that without the effect of the vertical walls, the vertical component of the vorticity (ζ) is null everywhere. This situation has been pointed out by Thess in [16]. Fig. (2d) shows the distribution of ζ on the free surface, and indeed all the variations are in the vicinity of the vertical walls. This is another indication that our calculation has been fairly accurate. We remark that the numerical calculation automatically selected the orientation of the diagonal valley. For a slightly different initial perturbation (e.g. different combination of Fourier modes) the diagonal valley could change to the other diagonal direction. Nevertheless, the pattern of triangular MB rolls is repeatable.

Figs. 3–5 show similar results for three, four and five-cell MB convection for the corresponding M_a and A_r. The patterns are combinations of triangles, squares, and wedge-shapes. Similar to the two-cell case, all patterns

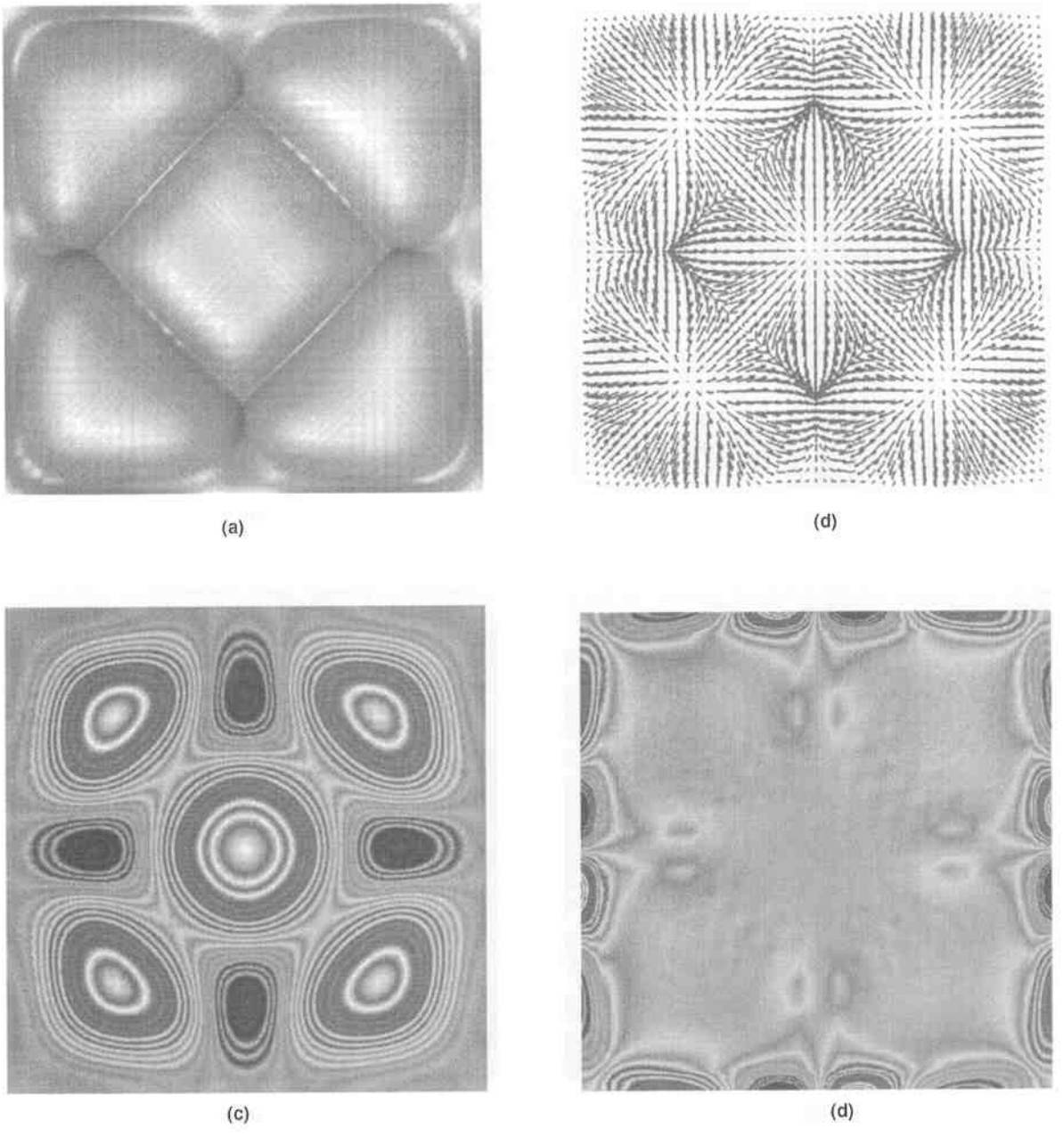

Fig. 5. The Marangoni–Benard convection in a square container with five cells for $M_a = 85$ and $A_r = 8.48$. (a) The pattern; (b) the velocity vectors on the free surface; (c) the temperature contours on the free surface; and (d) the vertical vorticity contours on the free surface.

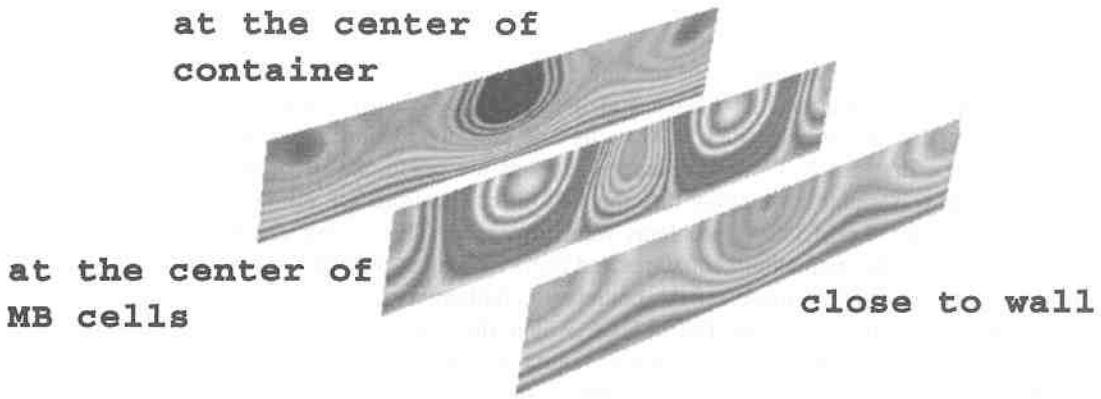

Fig. 6. The temperature contours on three vertical cross sections for the 4-cell case.

are repeatable with slightly different initial perturbations. The orientation of the pattern of three-cell case, however, could be different. Again, in all patterns, the centers of the MB rolls, where the fluid is drawn upward from the bottom, are always hotter than the valleys, where the colder fluid is pushed downwards to be heated up. The coldest regions of the flowfields are always at the intersections of several valleys. All these patterns have been observed in the laboratory by Koschmieder and Prahl [3]. Due to the existence of the vertical walls, these patterns are quite different from the general conception of the hexagonal MB convection usually observed in the containers with very large A_r.

To show the three-dimensional features of the flow fields, we plot vertical sections of the temperature profiles and velocity vectors for the 4-cell case. Fig. 6 shows three temperature profiles in the vertical sections: one crosses the center of the container, one crosses the center of a MB cell and the last one is close to the wall. For the 4-cell case, the coldest spot on the free surface is at the center of the container. These vertical cross sections show that the constant temperature contours of colder regions always have smaller opening on the free surface. However, the constant temperature contours of hot regions have larger openings on the free surface. This pattern is consistent with the simulation results shown by Thess [16]. Fig. 7 shows the velocity vectors of a vertical section crosses the center of two MB cells. It is obvious that there are two upwardly rising stream at the centers of the two cells. The colder fluid flows downward along the walls and the centerline to form several recirculation bubbles.

The critical Marangoni numbers M_{ac} for all these cases, i.e. $5.68 \leqslant A_r \leqslant 8.4$, lies between 80 and 85, which is consistent with the data reported by Koschmieder and Prahl [3]. For each A_r, the M_{ac} is obtained by starting the simulation with a small Marangoni number. Before the onset of the MB convection, the imposed perturbation always diminished as time progressed. We then increased the Marangoni number by a small number (usually 2 to 5) and ran the simulation again. We repeated the procedure until the imposed perturbation grew as time progressed and we knew that we had the onset of the MB convection and the critical Marangoni number for the specified A_r. For a Marangoni number close to the critical number for the onset of the convection, the flowfield was very unstable and changed randomly and it took a long time and many iterations for us to discern whether the perturbation was actually growing and reaching a certain pattern. This was a laborious and time consuming task. In this paper, we are contented with the unusual patterns obtained by the numerical simulations. In future work, we shall pursue detailed analysis of the transient phenomena.

Fig. 7. The velocity vectors on a vertical cross section across the centers of two MB rolls for the 4-cell case.

5. Concluding remarks

In this paper, we reported the simulations the three-dimensional Marangoni–Benard convection based on the LSFEM. The continuity equation, the Stokes equations, and the time-marching energy equation are solved simultaneously. Dependent variables such as vorticity and heat conduction fluxes are introduced to reduce the flow equations to be first order. These first-order equations are composed of several div–curl–grad systems. Facilitated by dummy variables, we show that the first-order equations are elliptic. As a result, the required boundary conditions for the MB flow problems were illustrated. This is crucial for the present calculations, because the coupling of the momentum equations and energy equation as well as the driving force of the whole flowfield depend on an accurate model of the boundary condition.

The equation set is solved by the LSFEM, in which the coefficient matrix is always symmetric and positive-definite. The inversion of the coefficient matrix is carried out by the JCG method, in which the computation is element-by-element and no assembly of the global matrix is needed. The MB convections in small square containers with two, three, four and five-cell MB convections are simulated. The obtained patterns are identical to that reported by Koschmieder and Prahl. The critical Marangoni numbers for all these cases are also consistent with their data.

Acknowledgments

The first author of this paper wants to thank Dr. David Jacqmin of the NASA Lewis Research Center for fruitful discussions. He also wants to thank Dr. A. Theses at Dresden University of Technology, Germany, for answering several questions that he had about the paper [16]. The financial support by the NASA Lewis Research Center monitored by Dr. Robert Stubbs is greatly appreciated.

References

[1] E.L. Koschmieder, J. Fluid Mech. 30 (1967) 9–15.
[2] E.L. Koschmieder and M.I. Biggerstaff, J. Fluid Mech. 167 (1986) 49–64.
[3] E.L. Koschmieder and S.A. Prahl, J. Fluid Mech. 215 (1990) 571–583.
[4] E.L. Koschmieder and D.W. Switzer, J. Fluid Mech. 240 (1992) 533–548.
[5] E.L. Koschmieder, Benard Cells and Taylor Vortices (Cambridge University Press, 1993).
[6] S.H. Davis, Ann. Rev. Fluid Mech. 19 (1987) 403–435.
[7] J.C. Legros, O. Dupont, P. Queeckers, S. van Vaerenberg and D. Schwabe, Prog. Astronaut. Aeronaut. 130 (1990) 207–239.
[8] J.R. Pearson, J. Fluid Mech. 4 (1958) 489–500.
[9] D.A. Nield, J. Fluid Mech. 19 (1964) 533–548.
[10] S.H. Davis, J. Fluid Mech. 39 (1969) 347–359.
[11] A. Cloot and G. Lebon, J. Fluid Mech. 145 (1984) 447–469.
[12] J.W. Scanlon and L.A. Segal, J. Fluid Mech. 30 (1967) 149–162.
[13] J.C. Duh, Int. J. Microgravity Res. Applic. VII(2) (1994) 98–102.
[14] K.H. Winters, Th. Plesser and K.A. Cliffe, Physica 29D (1988) 387–401.
[15] M. Bestehorn, Physical Review E 48(5) (1993) 3622–3634.
[16] A. Thess and S.A. Orszag, J. Fluid Mech. 283 (1995) 201–230.
[17] A. Thess and S.A. Orszag, Phys. Rev. Lett. 73(4) (1994) 541–544.
[18] S. Rosenblat, S.H. Davis and G.M. Homsy, J. Fluid Mech. 120 (1982) 91–122.
[19] S. Rosenblat, G.M. Homsy and S.H. Davis, J. Fluid Mech. 120 (1982) 123–138.
[20] J.C. Chen and J.Y. Chen, Linear Marangoni Instability of a Fluid in Cylindrical Containers, IAF-91-393, 42nd Congr. Int. Astronautical Federation, Montreal, 1991.
[21] B.N. Jiang, T.L. Lin and L.A. Povinelli, Comput. Methods Appl. Mech. Engrg. 114 (1994) 213–231.
[22] B.N. Jiang and L.A. Povinelli, Comput. Methods Appl. Mech. Engrg. 102 (1993) 199–212.
[23] S.T. Yu, B.N. Jiang, N.S. Liu and J. Wu, Int. J. Numer. Methods Engrg. 38(21) (1995) 3591–3610.
[24] S.T. Yu, B.N. Jiang, J. Wu and N.S. Liu, A div–curl–grad formulation for compressible buoyant flows solved by the least squares finite element method, Comput. Methods Appl. Mech. Engrg. 137 (1996) 59–88.
[25] S.T. Yu, B.N. Jiang, N.S. Liu and J. Wu, Simulation of an H_2/O_2 flame by the least squares finite element method, Int. J. Numer. Methods Fluids 23 (1996) 65–74.
[26] G.H. Golub and C.F. van Loan, Matrix Computations (The Johns Hopkins University Press, 1983).